ROYAL SOCIETY OF CHEMISTRY

PAPER

Check for updates

Additive engineering in $CH_3NH_3PbBr_3$ single crystals for terahertz devices and tunable high-order harmonics †

Sarvani Jowhar Khanam, [ID] [a] Srinivasa Rao Konda, [ID] *[b] Azmeera Premalatha,[a] Ravi Ketavath,[a] Wufeng Fu,[b] Wei Li [ID] *[b] and Banavoth Murali [ID] *[a]

Although organic–inorganic hybrid perovskites (OIHPs) are considered frontline candidates owing to their intriguing optoelectronic properties, their unstable surfaces are prone to degradation, significantly affecting device performance and hence limiting their commercialization. Additive engineering has become the most effective strategy to improve the quality of 3D perovskite single crystals (PSCs). Herein additive engineering employing various aliphatic, aromatic, and chiral ammonium salts results in high-quality transparent methylammonium lead bromide (MAPbBr₃) PSCs, which are demonstrated for application in terahertz (THz) devices, besides being sources for high-order harmonics generation (HHG). Remarkably the engineered crystal surfaces showed resistance to surface degradation compared to pristine ones, thereby enhancing the transmission/reflection of THz pulses. Moreover, a noticeable blue shift in harmonics (both nano second (ns) and pico second (ps) laser induced plasmas (LIPs)) was achieved compared to pristine MAPbBr₃ (MA). The current research is anticipated to open up new sources of additive-based SCs to be used entirely for THz devices and tunable high-order harmonic generation avenues. Exploring these inanimate materials *via* additive inclusion in MA SCs opens up new avenues to achieve blue-shifted UV spectra for diverse applications in attosecond physics and nonlinear spectroscopy, including tunable THz devices because of the easy tunability of the THz absorption properties, *i.e.* their phonon modes in an OIHPSC.

1. Introduction

Perovskite materials have attracted a lot of interest in optoelectronics research, such as photovoltaics,[1–5] light-emitting diodes (LEDs),[6–10] memristors,[11] lasers[12,13] luminescent solar concentrators,[14] and detectors,[3,15–22] owing to their promising optoelectronic properties and practical processability.[23–28] The tuneable bandgaps from 1.48 to 1.62 eV and >2.23 eV make OIHPs alluring semiconductors suitable for photovoltaic application and higher energy radiation detection (HERD), respectively.[20,21,29,30] Notably, surface quality is paramount to the efficacy of numerous device applications. The surface quality, crystallinity, and morphology of single crystals mainly

depend on PSC growth techniques,[31] including solvents,[32] the concentration/composition of the precursors,[33,34] annealing temperature,[31,32,34,35] and time duration for crystal growth.[35] So far, various crystallization techniques have been reported, including the inverse temperature method (ITC),[36] the temperature lowering method,[37] and the anti-solvent vapour assisted method (AVC).[38,39] A comprehensive comparison of PSCs and their applications has been tabulated in the electronic supporting information (ESI,† Table S1). Nevertheless, PSC performance, surface stability[40,41] and hysteresis[42–44] are pressing challenges for commercialization. The present article is focussed on a study of the effect of additives on surface degradation, and THz and HHG performance.

The additive engineering method is a versatile approach to growing more stable, high-quality PSCs, which has been explored further in the case of the synthesis of 2D and quasi-2D perovskite materials.[16,29,45–49] Fu *et al.* studied second harmonic generation circular dichroism (SHG-CD) in one dimensional (1D) [[R/S]-3-aminopiperidine]PbI₄.[50] On the other hand, terahertz (THz)-wave absorption properties in a mixed phase of 3D FAPbI₃ with theoretically performed (*ab initio*) calculations was demonstrated by Maeng *et al.*[51]

[a] *Solar Cells and Photonics Research Laboratory, School of Chemistry, University of Hyderabad, Hyderabad 500046, Telangana, India. E-mail: murali.banavoth@uohyd.ac.in*

[b] *The GPL Photonics Laboratory, State Key Laboratory of Luminescence and Applications, Changchun Institute of Optics, Fine Mechanics and Physics, Chinese Academy of Sciences, Changchun, 130033, China. E-mail: ksrao@ciomp.ac.cn, weili1@ciomp.ac.cn*

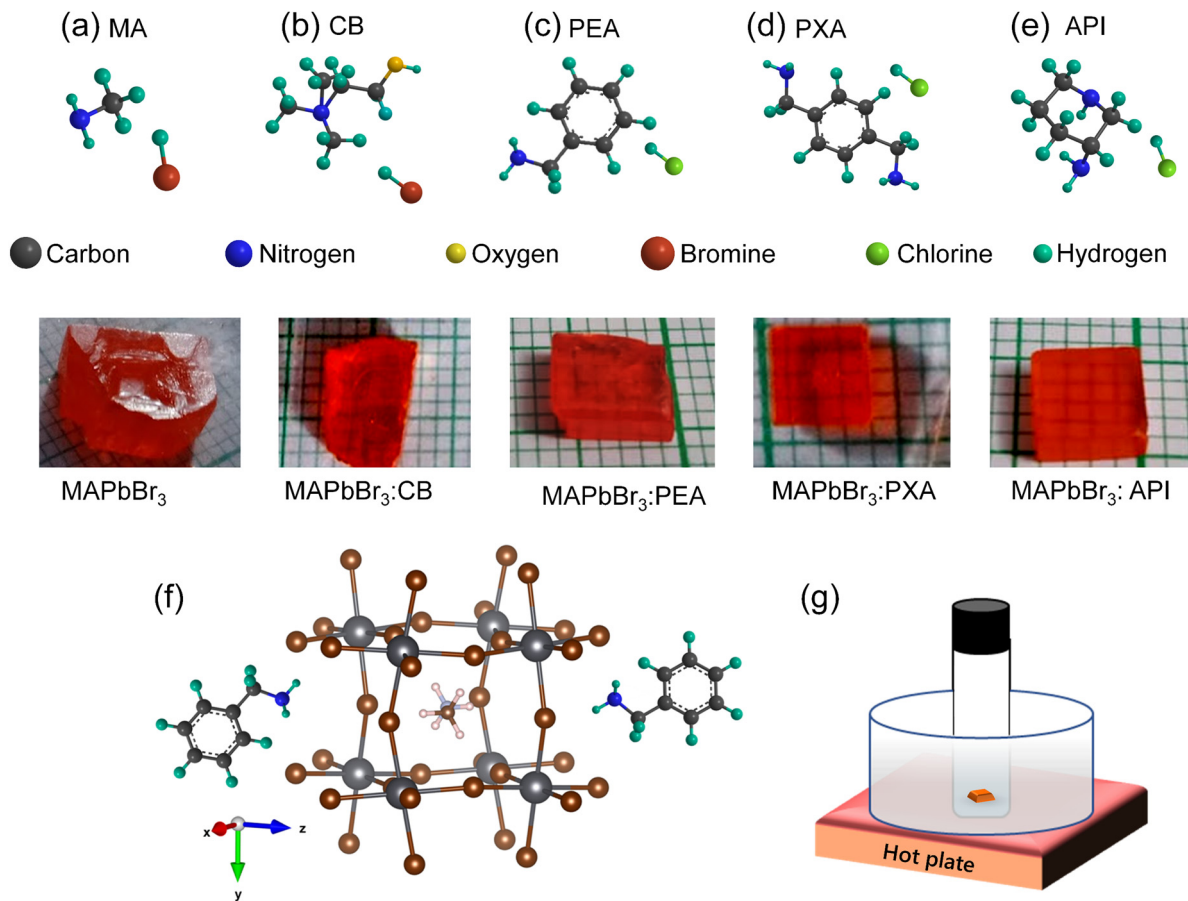† Electronic supplementary information (ESI) available. See DOI: https://doi.org/10.1039/d2tc05138a

Fig. 1 (a–e) Stuctures of additives used and photographs of the PSCs with labels at the bottom. (f) Possible model for additive coordination with unit cell during crystal growth process in solution. (g) ITC method used for crystal growth.

Herein, the current work aimed to study the changes in THz and HHG properties by changing the additives in 3D MA SCs grown using the additive engineering method (ESI,† Table S1). Therefore, we have taken different ammonium salts as additives (A) to investigate their role in preventing PSC degradation. We used the ammonium salts of the following types – aliphatic: choline bromide (CB), aromatic: phenylethylamine hydrochloride (PEA), p-xylylenediamine (PXA), and heterocyclic: (R)3-aminopiperidine dihydrochloride (API) – as additives, and labelled the respective crystals as MA:A (A = CB, PEA, PXA, API). Images of the crystals obtained are presented in Fig. 1(a)–(e). The effect of the interactions of the additives on the morphological, optical and surface properties of 3D PSCs is obscure and has yet to be explored for THz and high-order harmonic generation (HHG) applications. Herein, our work is focused on designing stable 3D MAPbBr$_3$ (MA) PSCs using the additive engineering method as reported elsewhere in the literature for 2D materials[16,29,45–49] and the structure–property–performance correlations between pristine (MA) and modified PSCs.

Furthermore, the HHG of these PSCs from their laser-induced plasmas (LIPs) was studied using 800 nm and 35 fs as the driving pulse (DP) and heating pulses (HP) of 800 nm, 200 ps and 1064 nm, 6 ns. Recently, we demonstrated the high-order harmonics from LIPs of Ni-doped CsPbBr$_3$ 2D nanocrystals with an average size of 20 nm using different DPs and LIPs created by the same HP and explained how the Ni-dopants play a crucial role in enhancing the harmonics and their cut-off.[52,53] Generally, blue shift of the harmonics could be achieved for a particular DP with negative chirps.[53–56] Interestingly, in the current scenario, the blue shift of the harmonics is obtained thanks to the influence of the additives on MA SCs.[57–60] The experimental layouts for THz-time-domain spectroscopy (THz-TDS) and HHG generation from LIPs of the reported PSCs are shown in Fig. S1(a) and (b) (ESI†). A detailed description of both setups is given in the ESI.†
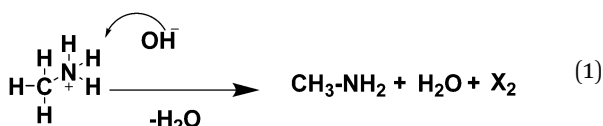
2. Results and discussion

2.1. Morphology and structural properties

One significant challenge is associated with the surface sensitivity of these PSCs to high levels of relative humidity (RH ≥ 55%) as the surface transforms and becomes disordered due to hydration, masking its actual properties. Recent reports have revealed from SEM images that exposure to humidity for several days results in the surface degradation of thin films.[61] However, for PSCs, it has been found that their surface properties differ

9938 | J. Mater. Chem. C, 2023, **11**, 9937–9951

This journal is © The Royal Society of Chemistry 2023

from bulk properties, including morphology, absorption coefficients, carrier mobility, photocurrent, carrier dynamics and optical bandgap. Such effects have been marginally exploited in PSCs with changing additives; therefore, the surface recombination losses, which play a decisive role in determining the intrinsic optoelectronic properties, must be fully understood.

While MABr is a hygroscopic salt, in ambient conditions it absorbs moisture and is converted to MA, leaving a $PbBr_2$ crystal surface or a vacant surface. Typically, $PbBr_2$-rich textures with pinholes and hydrate phases are formed. The N-based additives interact differently with the facets and have higher stability than their MABr counterparts. Hence, the surface degradation of modified and pristine PSCs by the environment has been studied using SEM measurements under exposure to ambient air. Confocal and SEM micrographs were recorded on the surface of fresh PSCs (Fig. S3(a)–(j), ESI†).

Furthermore, to study the change in morphology and pinholes after exposure to ambient conditions for three and seven days, SEM images were collected (Fig. S4(a)–(j), ESI†). Lower surface roughness has been observed for additive-based PSCs compared to pristine MA; this implies that the additives act as adequate passivating layers on the crystal surface. The chemical reaction on the surface of the crystal is shown below in eqn (1):

$$H_3C-\overset{\overset{\displaystyle H}{|}}{\underset{\underset{\displaystyle H}{|}}{N^+}}-H \ \xrightarrow[\text{-H}_2\text{O}]{OH^-} \ CH_3\text{-}NH_2 + H_2O + X_2 \tag{1}$$

The attachment energy (AE) model developed by Hartman and Bennema helps predict how additives interact with the surface of the growing facets and SC shape.[62,63] The AE of a facet is the energy released when layers of atoms are attached to the growing PSC surface; this energy depends on the bonding strength and number of bonds at a given facet. A possible mechanism for the additive engineering method can be explained using the model in Fig. 1(f), where the positively charged ammonium group coordinates with Br^- ions on the growing facet surface (with electrostatic interactions). This subsequently blocks the incoming $CH_3NH_3^+$ (methyl ammonium ion) or Pb^{2+} and maintains the same AE all over the growing facet (Fig. 1(f)). Herein, the strength of interaction between the ammonium ion and the facet decides the final quality of the crystal, which depends on the number of hydrogen bonds and electron density around the ammonium ion. Previous reports concluded that heterocyclic amine could effectively coordinate with a growing facet of the crystal, resulting in lower defects and enhancing crystallinity without altering the unit cell structure.[16,64–67] In Table 1, we have demonstrated the possible number of active groups with elements and the number of H-bonds among all the additives. The API additive can coordinate more effectively among all the additives owing to it having more electron dense groups around the N atom (+I inductive groups are present) and it can form 5 H-bonds more effectively with less steric hindrance. Cuboid, transparent, modified PSCs with lower roughness were obtained without any

Table 1 The possible active groups and H-bonds in the additives

Additive	Number of active groups (elements)	Possible number of H-bonds
CB	2[a] (3° N, O)	3
PEA	1[a] (1° N)	3
PXA	2 (1° N)	6
API	2[a] (2° N, 1° N)	5

[a] Primary (1°), secondary (2°) and tertiary (3°) amines.

polishing to improve the crystal surface quality (Fig. 1(a)–(e)).[68,69] Interestingly, we observed enhanced optical and THz transmission properties, as will be elaborated on in the subsequent experimental results.

Furthermore, to study the traces of hydrate phase and chemical state behaviour on the PSC surface, XPS studies were conducted. Interestingly, a single peak was observed in the C 1s and N 1s core-level bonding state chemical behaviour of MA-API SCs, indicating no new chemical state (Fig. 2a and b). On the other hand, more intense molecular defect peaks were seen in MA-PXA SCs. A striking shift towards higher energy was observed in the modified PSC Pb 4f core-level spectra, as shown in Fig. 2c, attributed to the increased binding energy and decreased halide vacancies.[70–72] Additionally, we confirmed the difference in H-bond strength among the additives, depending on the chemical state shift seen for the Br 3d core-level spectra compared to the pristine crystal; this might be due to a decrease in the electron cloud around the halide ion.

Subsequently, oxygen levels in the modified crystals were minimal, indicating the passivating nature of the additives and the presence of the hydrate phase on the crystal surface, which shows the main component around 532 eV corresponding to O–H, as discussed above.[73] It should be noted that an increase in oxygen concentration is linked with the breakdown of MABr to CH_3NH_2 and HX, which destroys the perovskite structure by deeper incorporation into PSCs, which is consistent with the long-exposure PSC SEM images.[73] Detailed XPS analysis of these modified PSCs indicated that the additive engineering method allows the formation of fewer molecular defects. Among all the modified PSC surfaces, it is evident that CB, PEA and API effectively passivated the surface and decreased the trap density, which is consistent with the SCLC measurement values.

We conducted powder XRD to determine whether additives were incorporated deeper into the lattice crystal lattice. Interestingly, no additional peak was observed relating to additives (Fig. 3(a)). Instead, increased peak intensities and a slight shift in the diffraction peaks to lower angles in the modified PSCs were observed (from 15.621° to 14.688° for the API-MA crystal) with increased peak intensity. This might be attributed to non-preferential crystal growth in all directions with higher crystallinity.[74] The peaks at $2\theta = 15.62°$, 30.77°, 46.62° correspond to the Miller indices of (100), (200), and (300) of the MA PSC, matching previously reported data.[38,75–78] Notably, the negative strain values in the case of MA-API SCs indicate lower ionic vacancies and compositional uniformity (Fig. S2(b), ESI†).[69–72]
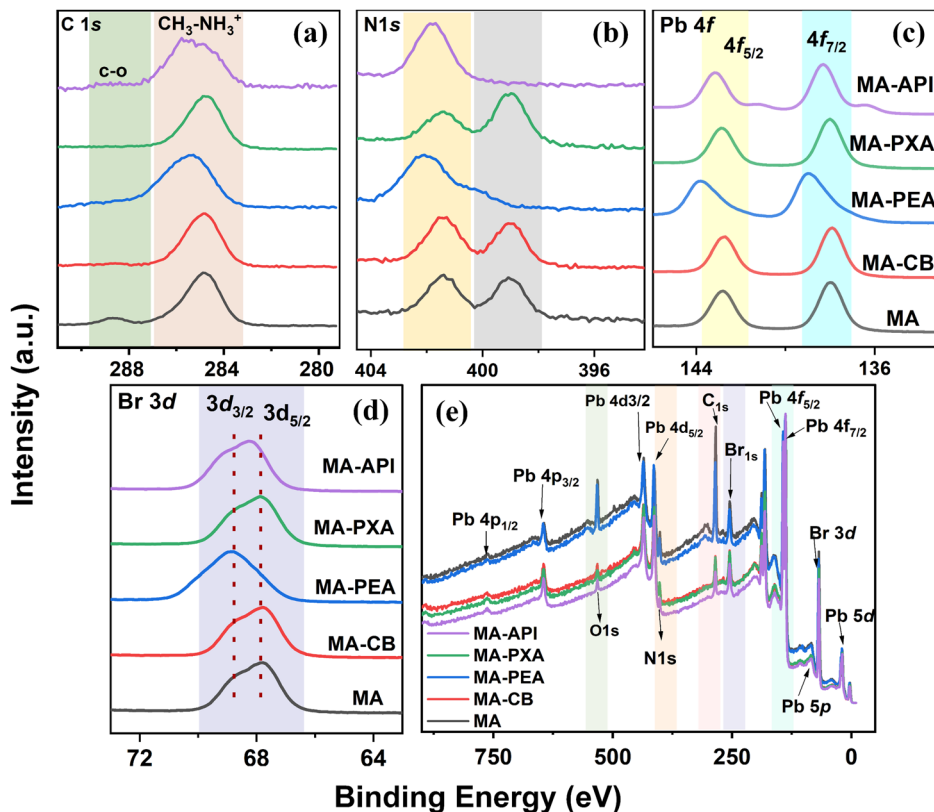
This journal is © The Royal Society of Chemistry 2023

J. Mater. Chem. C, 2023, **11**, 9937–9951 | **9939**

Fig. 2   (a–d) XPS data of C 1s, N 1s, Pb 4f and Br 3d core-level spectra with molecular level defect and chemical state behaviour in MAPbBr$_3$ SCs with changing additives (labels are shown on the right-hand side, following the same order (a–d)). (e) XPS survey spectra.
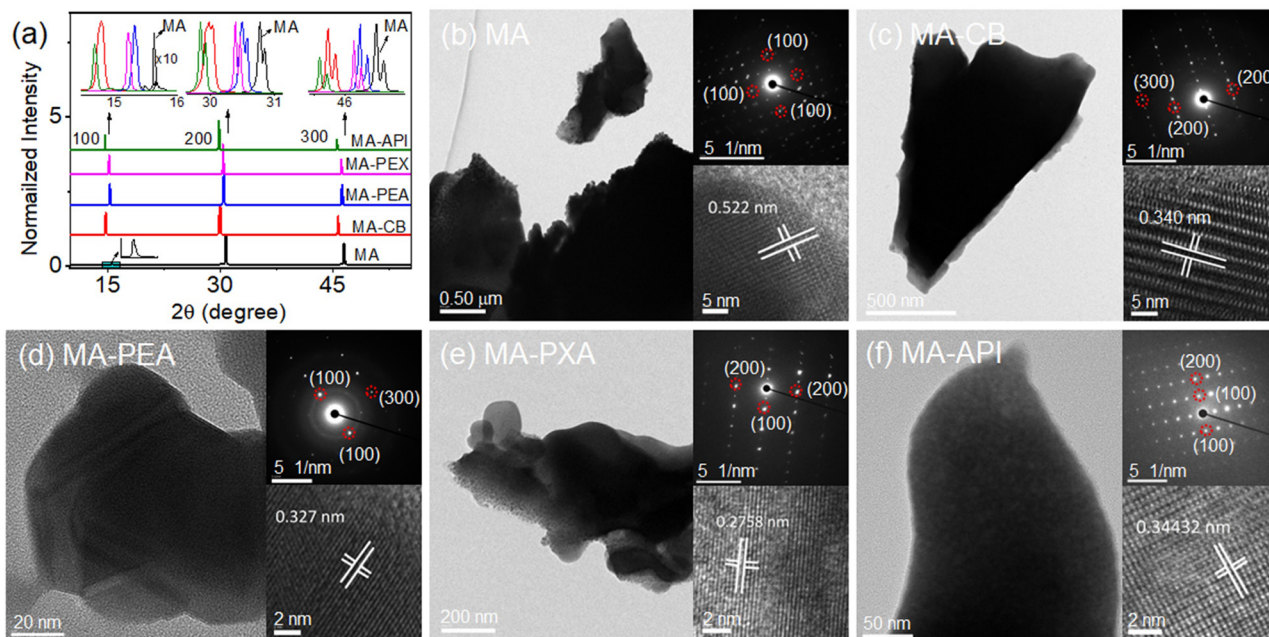

Fig. 3   (a) XRD patterns of typical MAPbBr$_3$ SCs grown by the additive-based ITC technique. (b–f) TEM images of pristine and modified PSCs.

The single-crystal X-ray diffraction (SC-XRD) data for MA and modified PSCs were also collected at 25 °C. Subsequently, data processing and indexing were automated within CrysAlis Pro software, and these results converge to a cubic cell for MA SCs

refined in the cubic space group $Pm\bar{3}m$ similar to that reported by Baikie *et al.*[79] However, no change in unit-cell was observed by changing the additives, which may be indicative that the additives act as a passivating layer on a surface without disturbing the unit-cell structure (Table S3, ESI†).

Subsequently, higher-resolution transmission electron microscopy (HR-TEM) of the PSCs was performed to study the changes in the SAED pattern with different additives (Fig. 3(b)–(f)). The HR-TEM image of MA provides lattice fringes at ~ 0.522 nm, related to the (200) planes of the cubic structure, close to the calculated value from powder XRD using the Bragg diffraction equation. The SAED result for pure SCs agrees with the reported data.[80–82] The TEM images of pristine and modified PSCs were collected from various spots on the grid (as the samples were very sensitive to incoming electrons).

2.2. Optical properties

Steady-state absorption spectra of the crystals were collected from the diffuse reflectance mode (DR). A slight change in the bandgap (E_g) of MA, MA-CB, MA-PEA, MA-PXA, and MA-API was observed at 2.178, 2.174, 2.176, 2.176, and 2.182 eV, respectively. (Fig. 4(a)). However, a decrease in halide vacancies and incorporation of Cl might be attributed to a change in the bandgap of the modified crystals. In this work, the bandgap values for MA SCs are similar to those in earlier work reported in the literature.[28,32] In most of the literature, perovskite optical stability was studied under atmospheric conditions with time duration of light exposure, at a particular temperature or by changing the temperature.[83,84] Herein, we have measured perovskite stability in the ambient atmospheric conditions (RH 76%, normal room light illumination) at different time intervals at 60 °C. (Fig. S5(a)–(e), ESI†). Subsequently, we carried out TGA measurements to check the thermal stability of the SCs. All the above evidence shows that MA-API is quite significantly stable and API acts as a more effective passivating layer on the surface (Fig. S6(a)–(b), ESI†).

The photoluminescence spectra (PL) were recorded using 405, 488 and 800 lasers. Interestingly, a shift in the peaks towards a high wavelength (from 520 nm to 579 nm for MA) was observed. Single photon absorption (1PA) (at 488 nm and 405 nm) and two-photon absorption (2PA) (at 800 nm) were used to photoexcite the surface and bulk PSCs to record the photoemission spectra.[74] The appropriate explanation for a shift in PL peak position with 2PA in comparison to 1PA could be due to the following factors: (a) the reabsorption of bulk emission by the thick PSC on route to the detector resulting in the absorption of the high-energy region of the emission spectrum, which is minimal;[85,86] (b) the band shift from the bulk to the surface.[87] A blue shift in steady-state PL spectra for modified crystals in the case of 1PA indicates fewer ionic vacancies (causing trap states), as discussed for the XPS data. The PL values for pristine PSC agree well with those of reported crystals grown by ITC and AVC methods (Fig. 4(b)).[32,88–90] Modified PSCs showed a slight change in optical properties, as confirmed from steady-state PL. Transient evolution of the electron–hole population after impulsive photoexcitation can
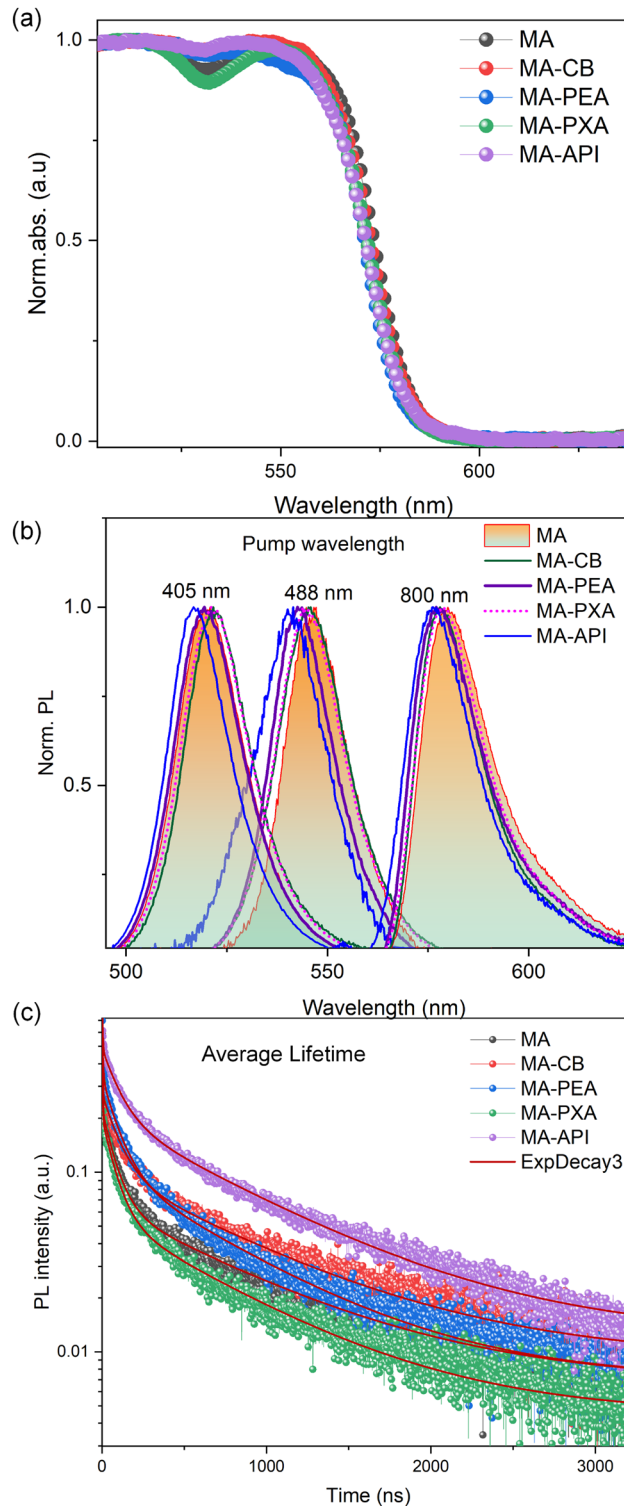

Fig. 4 (a) UV–visible spectra, (b) photoluminescence spectra with 1PA and 2PA photoexcitation and (c) average lifetime of MAPbBr$_3$ SCs with various additives.

be calculated from time-resolved photoluminescence (TRPL) measurements (Fig. 4(c)). Subsequently, the decay curves of the excited carrier in the modified PSCs were fitted using a tri-exponential decay model to quantify the carrier dynamics, and

This journal is © The Royal Society of Chemistry 2023

J. Mater. Chem. C, 2023, **11**, 9937–9951 | **9941**

Table 2 Comparative study of PSC fitted parameters for the TRPL decay profiles, V_{TFL} and η_{traps}

PSCs	τ_1 (ns)	τ_2 (ns)	τ_3 (ns)	τ (ns)	V_{TFL} (V)	η_{traps} ($\times 10^{10}$ cm^{-3})
MA	2.48	80.11	857.37	2.48	1.67	5.24
MA-CB	2.47	101.08	864.96	2.14	1.64	5.16
MA-PEA	2.88	87.58	684.78	2.89	1.61	5.07
MA-PXA	2.41	81.35	765.30	2.41	2.96	9.28
MA-API	3.79	116.1121	949.014	6.25	1.53	4.79

RA = relative amplitude.

the fitted parameters are summarized in Table 2. The relatively faster decay components (τ_1 and τ_2) are attributed to charge carrier trapping defect states, while the slower decay components (τ_2) are assigned to bimolecular radiative recombination in the bulk crystals. In proportion to the fast decay component (τ_1), a slower trapping time constant (2.88 ns for MA-PEA and 3.79 ns for M-API) is observed, compared to that of the pristine PSCs (2.48 ns), which is indicative of a reduced density of defects. Furthermore, the τ_3 value increased from 857.37 ns (pristine) to 949.01 ns (MA-API), suggesting that the additives lengthen the charge carrier lifetimes within the bulk crystal. As a result, the average PL lifetime was significantly enhanced from 2.48 ns to 6.25 ns (MA-API) (Fig. 4(c)).[91,92] To reveal the difference in electronic properties with additives in-gap deep electronic trap states were measured using the current–voltage (I–V) response of the PSCs in the space-charge limited current (SCLC) regime for all PSCs(Fig. S7(a)–(e), ESI†). The SCLC

values obtained for MA and MA-API SCs are shown in Fig. 5(a) and (b). At low voltages, the I–V response was ohmic (i.e. linear), as confirmed by the fit to $I \approx V$ (n =1). At intermediate voltages, the current exhibited a rapid nonlinear rise. This signalled the transition to the trap-filled limit (TFL)—a regime in which the injected carriers filled all the available trap states and were linearly proportional to the density of trap states (η_{trap}). Correspondingly, we found remarkably low η_{traps} for modified PSCs (MA-API η_{traps} = 4.79 × 10^{10} cm^{-3}), which together with the extremely clean absorption and PL profiles point to a nearly defect-free electronic structure. The lower defect density might be the origin of the reduced charge carrier trapping. The V_{TFL} obtained for all the samples (Fig. S7(a)–(e), ESI†) with η_{trap} parameters are summarized in Table 2. This result suggests a more significant trap-induced recombination rate in the MA SCss, which have a much higher trap density than the MA-API SCs, which can be explained using a model (Fig. 5(c) and (d)).[92] A focused explanation of the change in photodetection properties with additives was given in our recently published work.[93,94]

2.3. THz spectroscopy

THz spectroscopy has been well explored in various scientific research fields.[95–100] The transmission and reflection of the reported PSCs were studied using THz-TDS, a well-known method to ascertain a material's response in the far-infrared (IR) to near microwave region (the THz region).
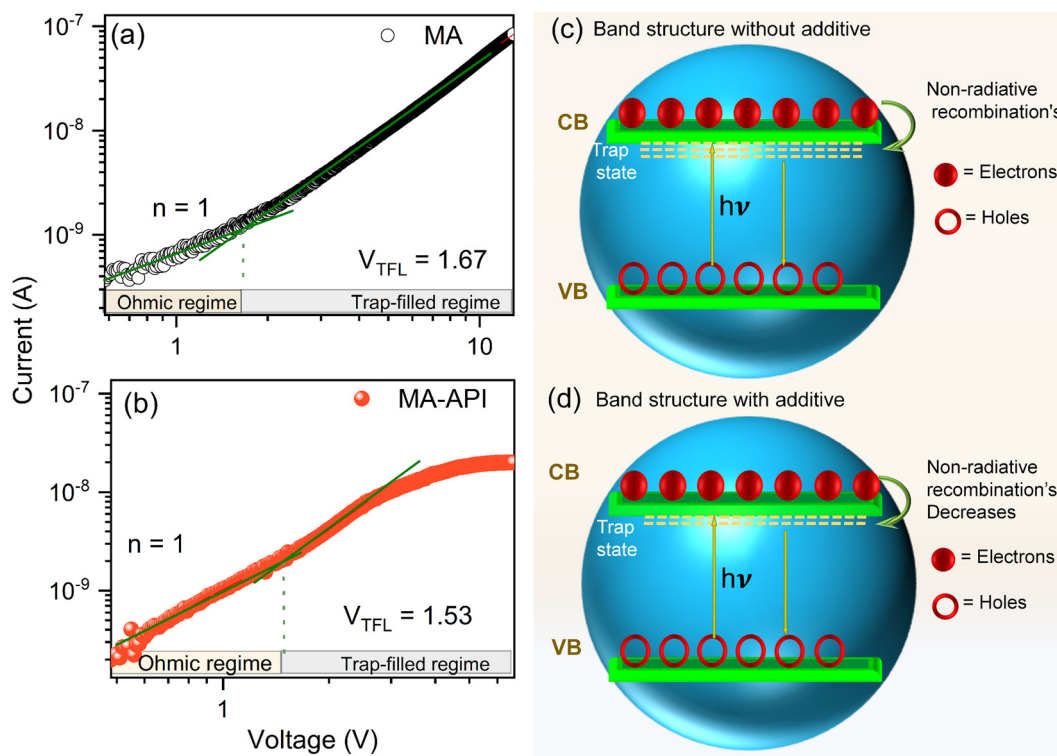

Fig. 5 (a and b) Current–voltage traces with V_{TFL}. The linear fitting is denoted with the green markers showing different regimes (at 300 K). (c and d) Electronic band structure model in pristine and modified PSCs represents decreasing surface defects by adding additives schematically.

9942 | J. Mater. Chem. C, 2023, **11**, 9937–9951

This journal is © The Royal Society of Chemistry 2023

We measured the transmittance, reflectance, and absorption coefficients of the PSCs (at a position of normal incidence to the THz pulses, referred to as $T@0°$). From the THz temporal profiles (electric field), one can obtain the real and imaginary refractive indices (n,k) and absorption coefficients using eqn (2)–(5) provided below. The complex FFT transmission data of the sample is compared to that of the reference given by

$$\frac{\psi_S}{\psi_{ref}} = \rho(\omega)e^{-i\phi(\omega)} \qquad (2)$$

where ψ_s and ψ_{ref} are the complex FFT of the sample (single crystals) and reference THz pulse, $\phi(\omega)$ is the phase difference (phase$_{amp}$–phase$_{ref}$), and $\rho(\omega)$ is the ratio of the peak amplitudes of the single-crystal and reference pulses (transmittance). The real part of the refractive index (n_S) and the imaginary part of the refractive index (k_S) can be written in terms of $\phi(\omega)$ and $\rho(\omega)$ as follows:[101,102]

$$n_S(\omega) = 1 + \frac{c_o}{\omega d}\phi(\omega) \qquad (3)$$

$$k_S(\omega) = \frac{c_o}{\omega d}\ln\left(\frac{4n_S(\omega)}{\rho(\omega)(n_S(\omega)+1)^2}\right) \qquad (4)$$

where c_o is the speed of light and d is the single-crystal thickness. From the imaginary part of the refractive index, one can determine the absorption coefficient α (cm^{-1}) as

$$\alpha(\omega) = \frac{2}{d}\ln\frac{4n_S(\omega)}{\rho(\omega)(n_S(\omega)+1)^2} \qquad (5)$$

Fig. 6(a) shows the THz electric field of the reference THz pulse (upper panel) and transmission ($T@0°$) from the five PSCs (bottom panel). The major THz pulse lies in the 2 to 3 ps range, and the PSCs show variations in the dip positions compared to the main reference pulse of around 2.4 ps. The THz transmission/reflection from the PSCs is measured by rotating them to 45° (referred to as $T, R@45°$) at normal incidence, and the obtained transmission/reflection THz electric field is shown in Fig. 6(b) and (c), respectively. To measure the transmittance/reflectance, n_s, k_s, and α, the amplitude and phase of the reference pulse and transmitted/reflected THz from the PSCs are important parameters. Therefore, we converted the THz electric field into a frequency domain using Fast Fourier Transform (FFT). In addition to amplitude and phase, we have shown the frequency in dB for three measurements, i.e. $T@0°$, $T@45°$ and $R@45°$ in Fig. S8(a)–(c) (ESI†), respectively. The ratios of amplitudes of reference and samples for three measurements are shown in Fig. 6(d)–(e). Whether in amplitude
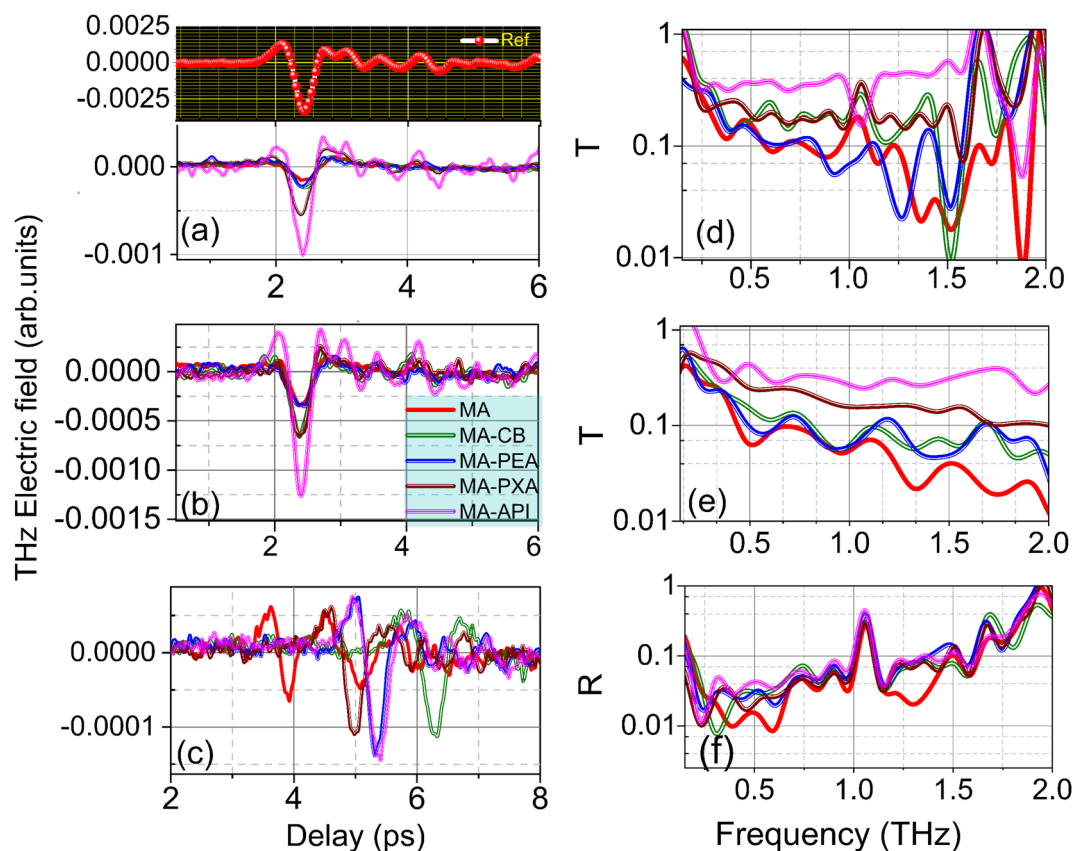

Fig. 6 (a–c) THz electric field (temporal profile) and (d–f) measured transmittance (T) $T@0°$ and $T@45°$ and reflectance (R) $R@45°$, respectively. The legend shown in (b) is applicable to all panels: red solid line, green double line, blue thick–thin lines, wine thin–thick lines, and magenta triple lines correspond to MA, MA-CB, MA-PEA, MA-PXA, and MA-API SCs, respectively.

This journal is © The Royal Society of Chemistry 2023

J. Mater. Chem. C, 2023, **11**, 9937–9951 | **9943**

(Fig. S8(a), ESI†) or frequency spectra in dB (Fig. S8(c), ESI†), or the transmittance/reflectance (Fig. 4(d)–(e)), the modified PSCs showed enhancement in THz transmission/reflection compared to pristine MA. Meanwhile, it is observed that this increment is not only connected to overall THz pulses; the modified SCs have a massive impact on the bandwidth (full width at half maximum (FWHM) for the transmitted and reflected THz pulse from PSCs) and variations in the central frequencies of the THz pulses. In this regard, we have fitted the THz amplitude data shown in Fig. S8(d) (ESI†) with Lorentz fits to obtain the central frequency and FWHM of the THz pulses (Fig. 7(a)). Here, it can be seen that the tendency of the central frequency and FWHM is to increase from MA to MA-API PSCs. These results indicate that the transmittance and reflectance are increased for modified SCs and follow
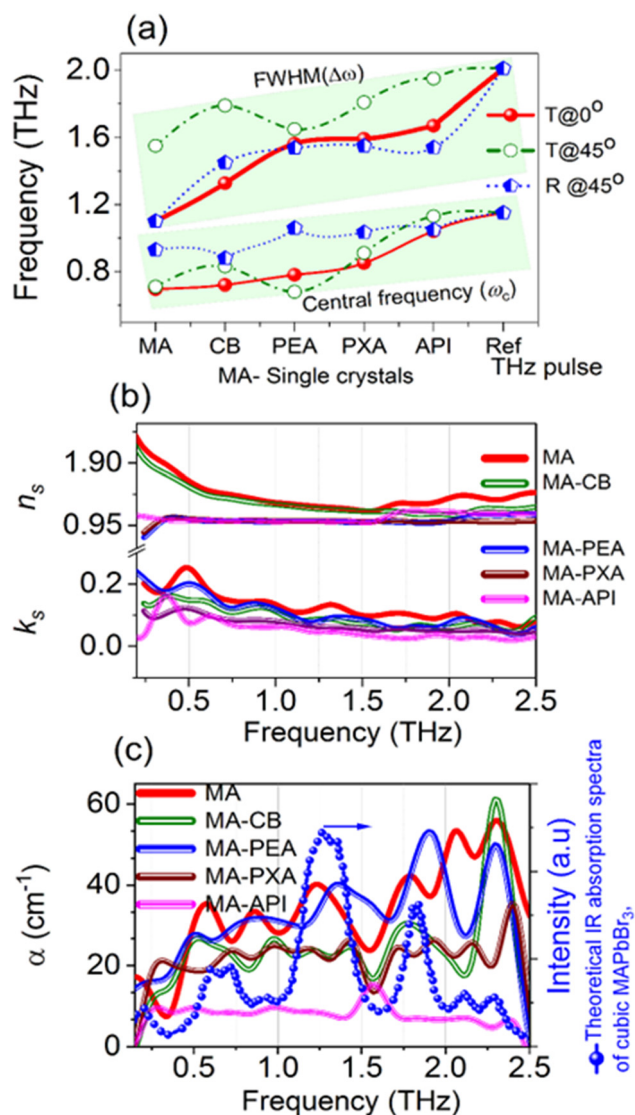
the order MA < MA-CB < MA-PEA < MA-PXA < MA-API. Therefore, it is reasonable to establish that the minimum crystal defects with good surface quality enhanced the optical and structural properties in the modified SCs. Furthermore, this can be reflected in the measured real and imaginary refractive indices shown in Fig. 7(b). It is found that the n_s values are higher than the k_s values (where k_s is related to the amount of absorption), which indicates that the samples possess an ordinary refractive index and show a small amount of absorption (the k_s values are non-zero). If the k_s value is 0, the material is non-absorbing. However, for the studied PSCs, the crystals show considerable absorption because the k_s values are non-zero (Fig. 7(b), bottom panel). Subsequently, we measured the absorption coefficient (α) using the experimental THz-TDS data at $T@0°$ using eqn (5), as shown in (Fig. 7(c), left-hand Y-axis) and compared the phonon vibrations of the reported PSCs[101,102] with theoretical IR absorption spectra of cubic MAPbBr$_3$, as earlier reported by Maeng et al.[72] and shown in (Fig. 7(c), right-hand Y-axis). The experimentally calculated absorption peak values of MA approximately match the theoretically predicted values.[72] However, in the case of the modified PSCs, the amount of absorption is decreased, with a slight difference in the peak positions.

In OIHPs, the organic unit undergoes molecular vibrations, leading to lattice vibrations due to a weak interaction between the organic and inorganic parts. Maeng et al.[72] demonstrated that molecular defects do not influence the three major phonon modes originating from the transverse vibration (0.8 THz) or longitudinal optical vibrations (1.4 THz) of the Pb–Br–Pb bonds and the optical Br vibration (2.0 THz). However, in the present case, the modified PSCs showed slight variations in the optical and vibrational frequencies due to changes in their interplanar distances. The powder XRD measurements in the present study revealed that the interplanar distance increased slightly for the modified SCs. Therefore, this might be a reason for the decrease in optical/vibrational absorption in the modified SCs compared to MA; the results are shown in Fig. 7(c). Interestingly, MA-API shows more negligible THz absorption, with peak positions at 0.48, 0.96, and 1.56 THz. At 1.56 THz, the other crystals do not show any peak positions. The THz peak amplitude curve for MA-API (magenta triple curve) is almost identical to the reference pulse (solid black line), having lower values, as shown in Fig. S8(a) (ESI†). Similarly, the absorption coefficients decreased for SCs grown in CB, PEA, and PXA additives. Overall, the THz measurements indicate that the modified SCs possess higher transmission and reflection than pristine MA, which offers advantages to utilizing these PSCs for THz devices.

2.4. Application of PSCs toward the generation of high-order harmonics generation

Currently, gases are frequently used as sources of HHG media.[103–105] A study of HHG experiments utilizing gases is rather limited because there are just a few different types of element in the gaseous state in nature. Hence, several researchers focused on demonstrating HHG from various solid and liquid elements.[106,107] The laser intensity utilized in the experiments is

Fig. 7 (a) The measured FWHM and central frequency of the reference THz pulse, transmitted and reflected THz pulses from the SCs. (b) The measured real refractive index (n_s) and imaginary refractive index (k_s) and (c) left-hand Y-axis; absorption coefficents (α) of single crystals at transmittance $T@0°$. (c) Right-hand Y-axis: theoretical IR absorption spectra of cubic MAPbBr$_3$ SCs (data is adapted from ref. 72).

9944 | *J. Mater. Chem. C*, 2023, **11**, 9937–9951

This journal is © The Royal Society of Chemistry 2023

constrained because of the damage threshold to the solid. The photon energy resulting from this method is not particularly high. Recently, strong mid-infrared laser pulses demonstrated HHG from MAPbX$_3$ (X = I, Br, Cl) thin films.[106,107] The near IR wavelength 800 nm is the current work-driving pulse, which possesses stronger energy than mid-infrared pulses. Therefore, there might be a chance of strong ablation leading to damage to the bulk PSCs. If we choose a DP laser energy below the damage threshold of PSCs due to the illumination of strong photoluminescence, the DP, along with the harmonics (if generated), will not transmit from almost 1 mm thick SCs. Therefore, in the present experiment, we pay attention to the method of LIPs [produced by 800 nm (200 ps) and 1064 nm (5ns) wavelengths] to generate harmonics from five bulk PSCs for the first time. Additionally, substantial resonance enhancement can be used to increase harmonic conversion efficiency by utilizing the HHG from LIPs of various metals.[108,109] The impacts of additives (CB, PEA, PXA, and API) on MA SCs were analyzed by measuring HHG spectra in terms of harmonic intensity, cut-off, and spectral shift. Initially, we describe the

stability of crystals, then the harmonic-cut-off and spectral shift in the following sub-sections.

2.4.1. Using harmonic intensity to describe the stability of PSCs. In the case of ps LIPs, a 2D color map of the harmonic spectra of PSCs for different DP intensities in the 1.5 to 9×10^{14} W cm^{-2} range (at a fixed ps HP intensity of 1.77×10^{10} W cm^{-2}) is shown in Fig. 8(a) and that for variation in ps HP intensities between 0.6 and 2.25×10^{10} W cm^{-2} at fixed $I_{DP} = 6 \times 10^{14}$ W cm^{-2} is presented in Fig. 8(b), and the corresponding maximum harmonic signals for the studied PSCs are shown in Fig. 9(a) and (b), respectively. With the increase in DP intensity, the modified SCs show a higher harmonic signal than pristine MA. The additives PEA, PXA, and API required a minimum of 3.0×10^{14} W cm^{-2} to obtain the harmonic spectra, whereas MA and MA-CB show the harmonic spectra even at 1.5×10^{14} W cm^{-2}. From Fig. 8(b) or Fig. 9(b), it can be observed that for MA SCs and MA-API, harmonic emission is obtained within the range of 0.6 to 2.25×10^{10} W cm^{-2}, whereas for MA-PEA, MA-CB, and MA-PEX, the harmonic emission was initiated at 1.05, 1.18
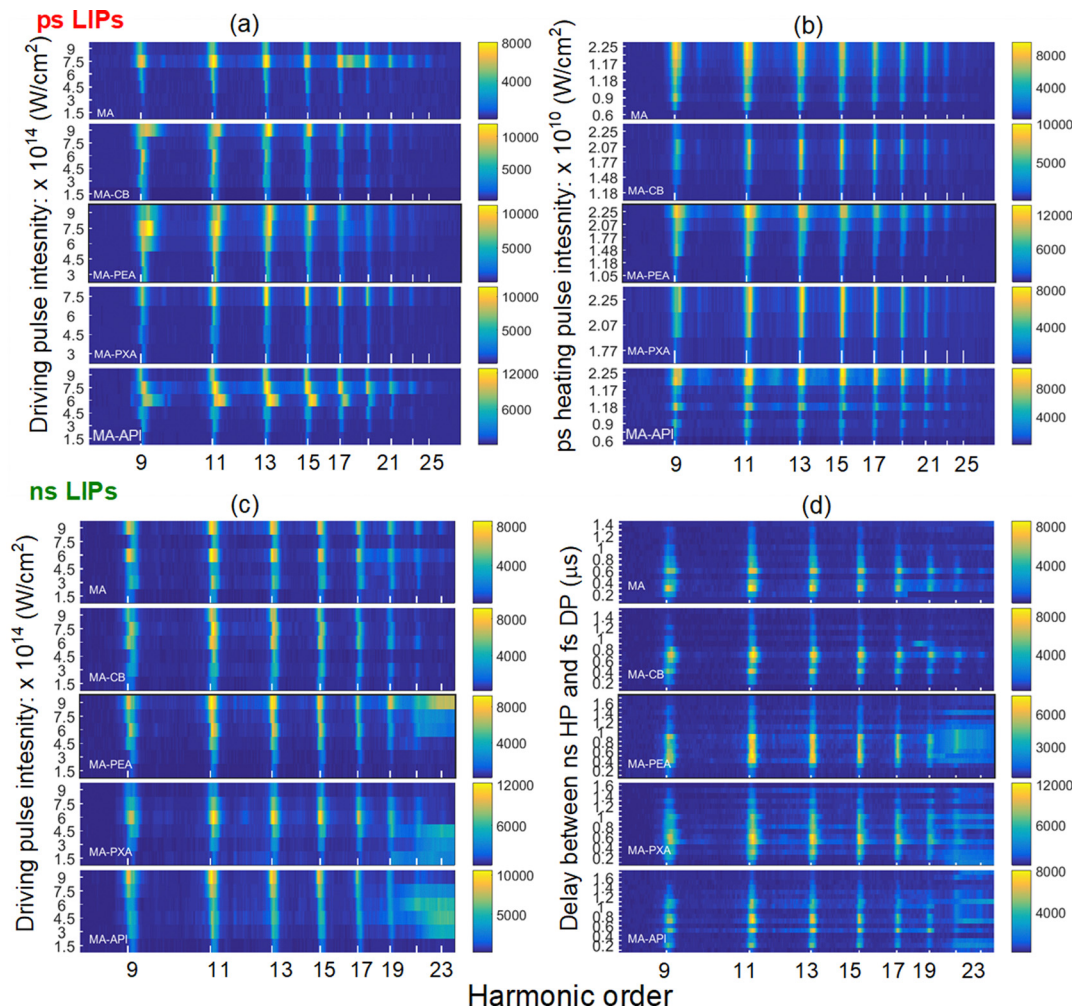

Fig. 8 2D colour map of harmonics spectra for different (a, c) driving pulse intensities (I_{DP}) for ps LIPs, at ps heating pulse intensity ($I_{ps,HP}$) = 1.77×10^{10} W cm^{-2}) and ns LIPs ($I_{ns,HP} = 7 \times 10^{10}$ W cm^{-2}), respectively, (b) at fs driving pulse intensity (I_{DP}) = 6.0×10^{14} W cm^{-2} w.r.t. ps heating pulse intensity ($I_{ps,HP}$). (d) The delay dependence between ns HP and fs DP.

This journal is © The Royal Society of Chemistry 2023
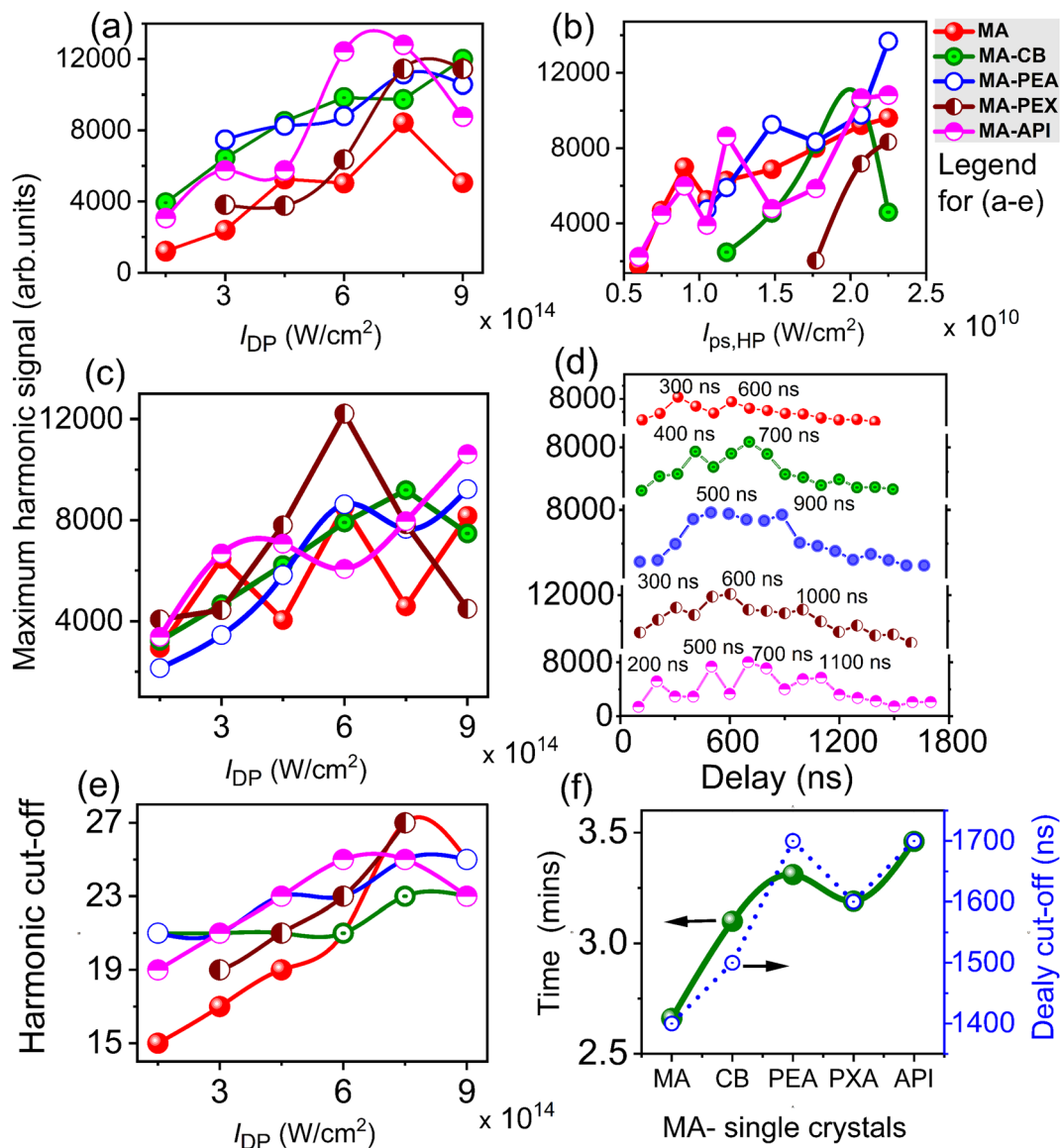
J. Mater. Chem. C, 2023, 11, 9937–9951 | 9945

Fig. 9 The maximum harmonic signal obtained (from data shown in Fig. 8(a–d)) for (a) at fixed ps heating pulse intensity ($I_{ps,HP}$) = 1.77 × 10^10 W cm^−2 for changes in driving pulse intensity (I_{DP}), (b) at fixed I_{DP} = 6.0 × 10^14 W cm^−2 with variation in $I_{ps,HP}$. In the case of ns LIPs (at $I_{ns,HP}$ = 7 × 10^10 W cm^−2) (c) w.r.t. I_{DP}, (d) the delay dependence between ns HP and fs DP, respectively. (e) Harmonic cut-off in the case of ps LIPs with changes in I_{DP}. (f) The cut-off of time duration until harmonic emission (left-hand Y-axis), and the delay cut-off (right-hand Y-axis) for the studied single crystals.

and 1.77 × 10^10 W cm^−2, respectively. This confirms that adding additives to MA increased the stability of the PSCs, which required a high intensity of ps pulses to create the plasma plumes. The maximum harmonic signal for additives PEA and API is slightly higher than for MA, whereas for CB and PEX, the intensity of the harmonic signal is less than that for MA.

Likewise, for the ps LIPs harmonic spectra from SCs (Fig. 8(a) and (b)), the harmonic emission from the modified crystals at a fixed ns HP intensity of 7 × 10^10 W cm^−2 compared with pristine crystals for different I_{DP} is shown in Fig. 8(c), and the delay dependence in harmonic spectra between ns HP and fs DP is shown in Fig. 8(d). The maximum harmonic signals obtained from these Fig. 8(c) and (d) HHG spectra are shown in

Fig. 9(c) and (d). In the case of ns LIPs, the intensities of the harmonics among the PSCs are very close to each other with respect to the increase in I_{DP} (at 6.0 × 10^14 W cm^−2 MA-PEX shows the highest intensity among them all). However, the advantages of ns HPs could be useful for measuring delay-dependent harmonic spectra. The additive-based PSCs increased the emission of harmonics at longer delays, as shown in Fig. 9(d). The cut-off delays were achieved at 1400, 1500, 1700, 1600, and 1700 ns for MA, MA-CB, MA-PEA, MA-PEX, and MA-API, respectively. Within these delay ranges, MA shows the first and second maxima of harmonics achieved at delays of 300 and 600 ns, respectively. At the same time, the maxima move for the modified PSCs. For MA-CB, MA-PEA, MA-PEX, and MA-API, the first maxima were presented at 400, 500, 600, and

9946 | J. Mater. Chem. C, 2023, **11**, 9937–9951

This journal is © The Royal Society of Chemistry 2023

700 ns, and the second maxima were obtained at 700, 900, 1000 and 1100 ns, respectively. Subsequently, in the case of MA-PEX, an additional maximum is presented at 300 ns; for MA-API, the maxima are located at 200 ns and 500 ns. The periodicity of the maximum harmonic signals indicates that the PSCs possess not only single component atoms or ions but small- to large-sized clusters produced by ns HP which travel at different velocities.

Overall, studies recording HHG spectra in the case of ps HP intensity variations and ns HP with delay dependence revealed that the modified SCs show higher stability than pristine MA. The stability of the SCs was also confirmed by ablating them with ns HP at a fixed position on the sample surface and collecting the HHG spectra within the exposure time (Fig. S9, ESI†). The harmonic spectra shown in Fig. S9(a) (ESI†) indicate that ablation of pristine MA continuously produced plasma plumes for 2.66 mins (frame rate 100 ns, saving five frames in 1 s using CCD). However, as shown in Fig. S9(b)–(e) (ESI†), MA-CB, MA-PEA, MA-PEX, and MA-API have some gaps in the presented harmonic spectra and extend the stability of the signal up to 3.10, 3.31, 3.19, and 3.46 mins, respectively. The gaps in the harmonic spectra for additive-based crystals revealed that plasma formation requires more ablating laser pulses. The cut-off of the time duration up to harmonic emission vs the studied SCs (Fig. 9) showed that the time duration

increased from MA to MA-API. This is direct evidence that modified SCs show longer stability than pristine MA with exposure to ns HP.

2.4.2. Harmonics cut-off. The maximum cut-off achieved for ns LIPs is close to 21 to 23H. As shown in Fig. 9(c), the cut-off of MA and MA-CB at $I_{DP} = 1.5 \times 10^{10}$ W cm^{-2} was 19H; this cut-off increased to 23H with an increase in I_{DP}. Similarly, MA-PEA, MA-PXA, and MA-API show almost 21H–23H [due to the appearance of plasma lines for these PSCs, 23H could not be seen in the HHG spectra of Fig. 8(c) panels 3 to 5 (from top to bottom)]. The HHG spectra for ns LIPs are only one order smaller than those for ps LIPs (25H). Earlier, we showed that in the case of Ni-doped CsPbBr$_3$, perovskite nanocrystals in the case of ps LIPs produce 27H and ns LIPs produce 21H using 800 nm DP.[52] In the present case for ps LIPs, the cut-off for five PSCs with respect to changes in I_{DP} is shown in Fig. 9(e). MA possesses a minimum cut-off at 15H and a maximum at 27H, and the modified MA SCs possess a higher cut-off at a lower I_{DP}. This indicates that the presence of additive plasma components might lead to an increase in overall density. As a result, a higher cut-off and highly intense harmonics are achieved for the modified SCs. The overall tendency of the harmonic cut-off, as shown in Fig. 9(e), is to increase with further growth in I_{DP}, because it is well known that energy cut-off is linearly proportional to the input-driving pulse intensity (as per the energy
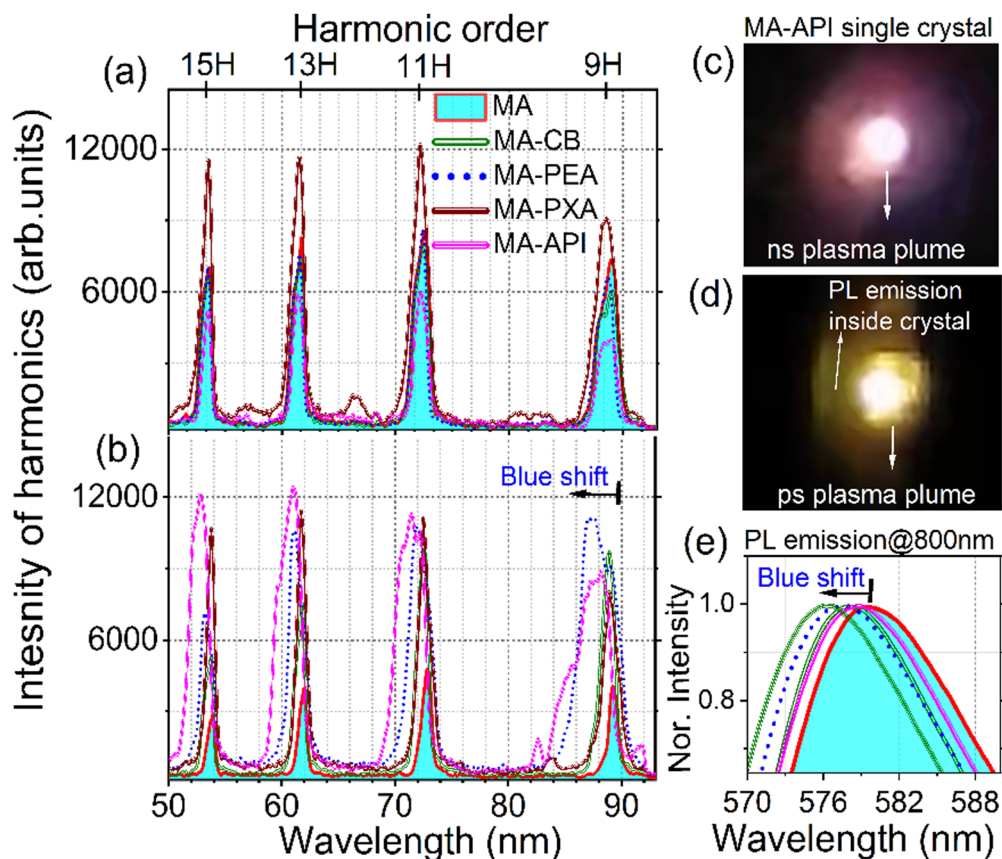

Fig. 10 HHG spectra 9H to 15H for (a) ns LIPs (b) ps LIPs at a driving pulse intensity of 6×10^{14} W cm^{-2}. For MA-API (c) plasma plumes obtained from ns HP, and (d) plasma plumes obtained from ps HP. (e) The normalized PL spectra at a pump wavelength of 800 nm.

This journal is © The Royal Society of Chemistry 2023

J. Mater. Chem. C, 2023, **11**, 9937–9951 | **9947**

cut-off formulae $E_{cut-off} = I_p + 3.17U_p$, where I_p is the ionization potential, and $U_p = 9.33 \times 10^{-14} I$ (W cm^{-2}) λ^2 (μm)).[110]

2.4.3. Spectral shift of harmonics. The intensity of ps HP variation and ns & fs delay-dependence studies does not influence the harmonic spectra in terms of their spectral shift. Because we have utilized the same I_{DP} for these measurements, the variation in I_{ps} and delay between ns and fs pulses leads to changes in the density of plasma components, which impacts the intensity of harmonics. However, a small clear blue shift in the harmonics is visible with respect to the variation in I_{DP} shown in Fig. 10(a) and (c) for ps and ns LIPs.

Generally, the blue shift of the harmonics could be achieved by changing the chirp of the driving laser pulses. The HHG spectra from the same material with variation in the DP intensity may not impose a shift in harmonics. However, in these modified PSCs, probably due to the presence of additive components leading to the variation in bandgap and crystallinity changes, it leads to interaction with the lower spectral components of DP 800 nm. This blue shift is more prominent in the case of ps LIPs than ns LIPs, as shown in Fig. 10(a) and (b). Fig. 10(a) and (b) show the 9H (88.88 nm), 11H (72.72 nm) to 13H (61.53 nm), 15H (53.33 nm) HHG spectra for ns LIPs and ps LIPs at a driving pulse intensity of 6×10^{14} W cm^{-2}, respectively. The shift of harmonics towards shorter wavelengths (blue shift) is more prominent for additive-based SCs. Fig. 10(c) and (d) show the plasma plumes formed by the ablation of MA-API SCs with ns and ps pulses. A similar pattern was achieved for all other PSCs. It is observed that with the ablation of ns pulses, only the plasma plumes expanded from the surface of PSCs. In the case of ps pulses, the PSCs themselves illuminate the green emission along with plasma plume expansion. In the case of ns pulses, with 1064 nm used as an ablating laser pulse, and for ps pulses, the excitation wavelength is 800 nm; due to the nonlinear absorption of 800 nm, there is PL emission. Therefore, it is assumed that the plasma components (atoms, ions, and nanoparticles) of PSCs may interact with the blue spectral components of 800 nm and decrease their harmonic wavelengths. Fig. 10(e) depicts the normalized PL spectra of PSCs measured at 800 nm, 35 fs, and 1 kHz pulses with an average power of 100 mW. This blue shift order of PSCs matches the HHG case and the order followed is MA-API > MA-PEA > MA-CB > MA-PXA > MA.

The presence of plasma components (atoms, ions, nanoparticles, and clusters) could be identified by an ICCD spectrometer. Meanwhile, It is well known that HHG is a three-step model:[111] (i) ionization by an intense laser field, (ii) acceleration in the laser field, and (iii) recombination with the parent ion leading to the generation of high-energy photons. The emission of high-order harmonics (high-energy photons corresponding to the driving laser field) is widely subject to the plasma components of PSCs. The emitted harmonics are a superposition of the individual contributions of each plasma component. The ionization potential (I_p) of the plasma components could influence the intensity and cut-off of the harmonics. The molecular formulae and the first and second ionization potentials of the five reported five PSCs are shown in Table S4 (ESI†). The MA and modified

PSCs have C, H, N, Pb, Br, O, and Cl chemical components. Among them, Pb has the lowest first ionization potential, *i.e.* 7.41 eV, by shortening the chemical components in ascending order according to their first ionization potential as Pb < C < Br < Cl < H < O < N. Interestingly, the Pb, Br and N weight percentages increase, and the C quantity decreases more than in MA (Fig. S2(a), ESI†). MA-CB has additional O, and MA-PEA, MA-PXA, and MA-API have additional Cl quantities compared to pristine MA. Therefore, it is expected that the modified PSC will contain a higher number of chemical components. Due to this, the plasma density (containing atoms and singly charged ions) will be higher in the case of these modified PSCs ablated by ns HP and ps HP. Therefore, the intensity of the harmonics, the cut-off (ps LIPs), and the spectral shift are higher for modified PSCs than for the pristine MA PSC. These parameters are significantly more affected in ps LIPs than in ns LIPs. Experimentally, we cannot directly differentiate or estimate the contributions of different plasma components. This is because we could not flexibly control the relative concentrations of the distinct charge states of ions that are always present in plasma. However, as mentioned above, we might estimate their contributions by assuming that the overall HHG yield is proportionate to the plasma density.

3. Conclusions

Understanding the surface properties of PSCs, including their crystallinity, surface qualities, and stability, is essential to improving the transmission of these crystals. Here, we directly visualized the surface transformation of a pristine PSC using spectroscopy and microscopy techniques. The results based on THz time-domain spectroscopy revealed that additive-engineered SCs could be prominent for applications in the THz regime. Out of all the additives used, the transmission/reflection of the THz pulse, higher intensity of the HHG signal and stability of the MAPbBr$_3$:API SC were improved in comparison to the pristine crystal because of effective passivation of the heterocyclic moiety (piperidine) with fewer molecular defects. Interestingly, a blue shift is also observed in the case of the HHG spectra of additive-based MAPbBr$_3$ SCs with DP 800 nm. HHG studies based on ps and ns LIPs found that additives such as CB, PEA, PXA and API increase the stability of SCs and are good emitters of HHG. Several pieces of evidence from our experimental results indicate that modified PSC surfaces with fewer defects have enhanced transmittance and structural properties compared to pristine MA. These findings open a new avenue for THz devices and tunable HHG applications using additive-based PSCs.

Author contributions

Sarvani Jowhar Khanam: conceptualization, data curation, investigation, formal analysis, methodology, writing – original draft, writing – review & editing. Srinivasa Rao Konda: conceptualization, data curation, investigation, analysis, initial draft, writing – review & editing. Azmeera Premalatha: formal analysis. Ravi Ketavath: formal analysis. Wufeng Fu: data

9948 | *J. Mater. Chem. C*, 2023, **11**, 9937–9951

This journal is © The Royal Society of Chemistry 2023

Conflicts of interest

There are no conflicts to declare.

Acknowledgements

References

1 Q. Dong, *Science*, 2015, **347**, 967–970.
2 K. Lin, J. Xing, L. N. Quan, F. P. G. de Arquer, X. Gong, J. Lu, L. Xie, W. Zhao, D. Zhang, C. Yan, W. Li, X. Liu, Y. Lu, J. Kirman, E. H. Sargent, Q. Xiong and Z. Wei, *Nature*, 2018, **562**, 245–248.
3 Y. Jia, R. A. Kerner, A. J. Grede, B. P. Rand and N. C. Giebink, *Nat. Photonics*, 2017, **11**, 784–788.
4 X. Jiang, X. Fu, D. Ju, S. Yang, Z. Chen and X. Tao, *ACS Energy Lett.*, 2020, **5**, 1797–1803.
5 B. Turedi, V. Yeddu, X. Zheng, D. Y. Kim, O. M. Bakr and M. I. Saidaminov, *ACS Energy Lett.*, 2021, **6**, 631–642.
6 M. Zhao, Q. Zhang and Z. Xia, *Mater. Today*, 2020, **40**, 246–265.
7 Y. Li, X. Zhang, H. Huang, S. V. Kershaw and A. L. Rogach, *Mater. Today*, 2020, **32**, 204–221.
8 Y. Li, I. Allegro, M. Kaiser, A. J. Malla, B. S. Richards, U. Lemmer, U. W. Paetzold and I. A. Howard, *Mater. Today*, 2021, **49**, 35–47.
9 S. Adjokatse, H. H. Fang and M. A. Loi, *Mater. Today*, 2017, **20**, 413–424.
10 J. Zhang, L. Wang, X. Zhang, G. Xie, G. Jia, J. Zhang and X. Yang, *Mater. Today*, 2021, **51**, 222–246.
11 J. Xing, C. Zhao, Y. Zou, W. Kong, Z. Yu, Y. Shan, Q. Dong, D. Zhou, W. Yu and C. Guo, *Light: Sci. Appl.*, 2020, **9**, 11.
12 G. Xing, N. Mathews, S. S. Lim, N. Yantara, X. Liu, D. Sabba, M. Grätzel, S. Mhaisalkar and T. C. Sum, *Nat. Mater.*, 2014, **13**, 476–480.
13 F. Deschler, M. Price, S. Pathak, L. E. Klintberg, D. D. Jarausch, R. Higler, S. Hüttner, T. Leijtens, S. D. Stranks, H. J. Snaith, M. Atatüre, R. T. Phillips and R. H. Friend, *J. Phys. Chem. Lett.*, 2014, **5**, 1421–1426.
14 P. Xia, S. Xu, C. Wang and D. Ban, *APL Photonics*, 2021, **6**, 120901.
15 F. Bai, K. Bian, X. Huang, Z. Wang and H. Fan, *Chem. Rev.*, 2019, **119**, 7673–7717.
16 Y. Feng, L. Pan, H. Wei, Y. Liu, Z. Ni, J. Zhao, P. N. Rudd, L. R. Cao and J. Huang, *J. Mater. Chem. C*, 2020, **8**, 11360–11368.
17 Y. Tang, M. Liang, M. Zhang, A. Honarfar, X. Zou, M. Abdellah, T. Pullerits, K. Zheng and Q. Chi, *ACS Appl. Mater. Interfaces*, 2020, **12**, 858–867.
18 C. Bao, Z. Chen, Y. Fang, H. Wei, Y. Deng, X. Xiao, L. Li and J. Huang, *Adv. Mater.*, 2017, **29**, 1–7.
19 Y. Liu, Y. Zhang, Z. Yang, D. Yang, X. Ren, L. Pang and S. F. Liu, *Adv. Mater.*, 2016, **28**, 9204–9209.
20 Q. Lin, A. Armin, P. L. Burn and P. Meredith, *Nat. Photonics*, 2015, **9**, 687–694.
21 F. Yao, P. Gui, C. Chen, B. Li, R. Li, C. Tao, Q. Lin and G. Fang, *ACS Appl. Mater. Interfaces*, 2019, **11**, 39875–39881.
22 P. Gui, Z. Chen, B. Li, F. Yao, X. Zheng, Q. Lin and G. Fang, *ACS Photonics*, 2018, **5**, 2113–2119.
23 Q. Huang, Y. Liu, F. Li, M. Liu and Y. Zhou, *Mater. Today*, 2021, **47**, 156–169.
24 F. Zhang, J. F. Castaneda, S. Chen, W. Wu, M. J. DiNezza, M. Lassise, W. Nie, A. Mohite, Y. Liu, S. Liu, D. Friedman, H. Liu, Q. Chen, Y. H. Zhang, J. Huang and Y. Zhang, *Mater. Today*, 2020, **36**, 18–29.
25 A. Bibi, I. Lee, Y. Nah, O. Allam, H. Kim, L. N. Quan, J. Tang, A. Walsh, S. S. Jang, E. H. Sargent and D. H. Kim, *Mater. Today*, 2021, **49**, 123–144.
26 T. H. Im, J. H. Lee, H. S. Wang, S. H. Sung, Y. Bin Kim, Y. Rho, C. P. Grigoropoulos, J. H. Park and K. J. Lee, *Mater. Today*, 2021, **51**, 525–551.
27 S. Sánchez, M. Vallés-Pelarda, J. A. Alberola-Borràs, R. Vidal, J. J. Jerónimo-Rendón, M. Saliba, P. P. Boix and I. Mora-Seró, *Mater. Today*, 2019, **31**, 39–46.
28 H. Zhang, M. K. Nazeeruddin and W. C. H. Choy, *Adv. Mater.*, 2019, **31**, e1805702.
29 N. Balis, A. A. Zaky, C. Athanasekou, A. M. Silva, E. Sakellis, M. Vasilopoulou, T. Stergiopoulos, A. G. Kontos and P. Falaras, *J. Photochem. Photobiol., A*, 2020, **386**, 112141.
30 L. Chao, Y. Xia, B. Li, G. Xing, Y. Chen and W. Huang, *Chem*, 2019, **5**, 995–1006.
31 Y. Liu, Y. Zhang, Z. Yang, J. Feng, Z. Xu, Q. Li, M. Hu, H. Ye, X. Zhang, M. Liu, K. Zhao and S. Liu, *Mater. Today*, 2019, **22**, 67–75.
32 M. I. Saidaminov, A. L. Abdelhady, B. Murali, E. Alarousu, V. M. Burlakov, W. Peng, I. Dursun, L. Wang, Y. He, G. Maculan, A. Goriely, T. Wu, O. F. Mohammed and O. M. Bakr, *Nat. Commun.*, 2015, **6**, 7586.
33 K. Schötz, A. M. Askar, W. Peng, D. Seeberger, T. P. Gujar, M. Thelakkat, A. Köhler, S. Huettner, O. M. Bakr, K. Shankar and F. Panzer, *J. Mater. Chem. C*, 2020, **8**, 2289–2300.

34 M. Ng and J. E. Halpert, *RSC Adv.*, 2020, **10**, 3832–3836.

35 J. Ding, Y. Zhao, S. Du, Y. Sun, H. Cui, X. Zhan, X. Cheng and L. Jing, *J. Mater. Sci.*, 2017, **52**, 7907–7916.

36 Y. Liu, Z. Yang, D. Cui, X. Ren, J. Sun, X. Liu, J. Zhang, Q. Wei, H. Fan, F. Yu, X. Zhang, C. Zhao and S. Liu, *Adv. Mater.*, 2015, **27**, 5176–5183.

37 Y. Dang, Y. Liu, Y. Sun, D. Yuan, X. Liu, W. Lu, G. Liu, H. Xia and X. Tao, *CrystEngComm*, 2015, **17**, 665–670.

38 D. Shi, V. Adinolfi, R. Comin, M. Yuan, E. Alarousu, A. Buin, Y. Chen, S. Hoogland, A. Rothenberger, K. Katsiev, Y. Losovyj, X. Zhang, P. A. Dowben, O. F. Mohammed, E. H. Sargent and O. M. Bakr, *Science*, 2015, **347**, 519–522.

39 A. Efrati, S. Aharon, M. Wierzbowska and L. Etgar, *EcoMat*, 2020, **2**, e12016.

40 R. K. Misra, S. Aharon, B. Li, D. Mogilyansky, I. Visoly-Fisher, L. Etgar and E. A. Katz, *J. Phys. Chem. Lett.*, 2015, **6**, 326–330.

41 G. Niu, X. Guo and L. Wang, *J. Mater. Chem. A*, 2015, **3**, 8970–8980.

42 S. van Reenen, M. Kemerink and H. J. Snaith, *J. Phys. Chem. Lett.*, 2015, **6**, 3808–3814.

43 S. R. Raga, M. C. Jung, M. V. Lee, M. R. Leyden, Y. Kato and Y. Qi, *Chem. Mater.*, 2015, **27**, 1597–1603.

44 Y. Han, S. Meyer, Y. Dkhissi, K. Weber, J. M. Pringle, U. Bach, L. Spiccia and Y. B. Cheng, *J. Mater. Chem. A*, 2015, **3**, 8139–8147.

45 C. Kuang, Z. Hu, Z. Yuan, K. Wen, J. Qing, L. Kobera, S. Abbrent, J. Brus, C. Yin, H. Wang, W. Xu, J. Wang, S. Bai and F. Gao, *Joule*, 2021, **5**, 618–630.

46 Y. Ma, Y. Cheng, X. Xu, M. Li, C. Zhang, S. H. Cheung, Z. Zeng, D. Shen, Y. Xie, K. L. Chiu, F. Lin, S. K. So, C. Lee and S. Tsang, *Adv. Funct. Mater.*, 2021, **31**, 2006802.

47 Z. Zhang, C. Xu, D. Wang, X. Zhang and J. Zhang, *J. Mater. Sci.: Mater. Electron.*, 2022, **33**, 3091–3100.

48 Y. Wang, X. Liu, T. Zhang, X. Wang, M. Kan, J. Shi and Y. Zhao, *Angew. Chem.*, 2019, **131**, 16844–16849.

49 L. He, Z. Xiao, X. Yang, Y. Wu, Y. Lian, X. Peng and X. Yang, *J. Mater. Sci.*, 2020, **55**, 7691–7701.

50 D. Fu, J. Xin, Y. He, S. Wu, X. Zhang, X. M. Zhang and J. Luo, *Angew. Chem., Int. Ed.*, 2021, **60**, 20021–20026.

51 I. Maeng, S. Lee, E. Q. Han, Y. Zhang, S. J. Oh, M. Nakamura, J.-H. Yun, L. Wang, Y.-K. Kwon and M.-C. Jung, *NPG Asia Mater.*, 2021, **13**, 75.

52 S. R. Konda, V. R. Soma, M. Banavoth, R. Ketavath, V. Mottamchetty, Y. H. Lai and W. Li, *ACS Appl. Nano Mater.*, 2021, **4**, 8292–8301.

53 S. R. Konda, V. R. Soma, R. A. Ganeev, M. Banavoth, R. Ketavath and W. Li, *J. Mater. Sci.*, 2022, **57**, 3468–3485.

54 M. Hussain, S. Kaassamani, T. Auguste, W. Boutu, D. Gauthier, M. Kholodtsova, J.-T. Gomes, L. Lavoute, D. Gaponov, N. Ducros, S. Fevrier, R. Nicolas, T. Imran, P. Zeitoun, G. O. Williams, M. Fajardo and H. Merdji, *Appl. Phys. Lett.*, 2021, **119**, 071101.

55 R. A. Ganeev, H. Singhal, P. A. Naik, U. Chakravarty, V. Arora, J. A. Chakera, R. A. Khan, M. Raghuramaiah, S. R. Kumbhare, R. P. Kushwaha and P. D. Gupta, *Appl. Phys. B: Lasers Opt.*, 2007, **87**, 243–247.

56 S. R. Konda, Y. H. Lai and W. Li, *Opt. Laser Technol.*, 2022, **146**, 107602.

57 S. Mikaelsson, J. Vogelsang, C. Guo, I. Sytcevich, A. L. Viotti, F. Langer, Y. C. Cheng, S. Nandi, W. Jin, A. Olofsson, R. Weissenbilder, J. Mauritsson, A. L'Huillier, M. Gisselbrecht and C. L. Arnold, *Nanophotonics*, 2020, **10**, 117–128.

58 S. Hadrich, M. Krebs, A. Hoffmann, A. Klenke, J. Rothhardt, J. Limpert and A. Tu, *Light: Sci. Appl.*, 2015, **4**, e320.

59 J. J. Li, J. Lu, A. Chew, S. Han, J. J. Li, Y. Wu, H. Wang, S. Ghimire and Z. Chang, *Nat. Commun.*, 2020, **11**, 2748.

60 N. Kanda, T. Imahoko, K. Yoshida, A. Tanabashi, A. Amani Eilanlou, Y. Nabekawa, T. Sumiyoshi, M. Kuwata-Gonokami and K. Midorikawa, *Light: Sci. Appl.*, 2020, **9**, 168.

61 B. Murali, E. Yengel, C. Yang, W. Peng, E. Alarousu, O. M. Bakr and O. F. Mohammed, *ACS Energy Lett.*, 2017, **2**, 846–856.

62 J. Li, C. J. Tilbury, S. H. Kim and M. F. Doherty, *Prog. Mater. Sci.*, 2016, **82**, 1–38.

63 P. Hartman, *J. Cryst. Grow.*, 1980, **49**, 166–170.

64 J. Gao, W. Zhang, Z. Wu, Y. Zheng and D. Fu, *J. Am. Chem. Soc.*, 2020, **142**, 6.

65 Y. Dang, X. Liu, Y. Sun, J. Song, W. Hu and X. Tao, *J. Phys. Chem. Lett.*, 2020, **11**, 1689–1696.

66 F. Zhang and K. Zhu, *Adv. Energy Mater.*, 2020, **10**, 1902579.

67 M. Mangrulkar and K. J. Stevenson, *Crystals*, 2021, **11**, 814.

68 T. Sekimoto, M. Suzuka, T. Yokoyama, R. Uchida, S. Machida, T. Sekiguchi and K. Kawano, *Phys. Chem. Chem. Phys.*, 2018, **20**, 1373–1380.

69 Q. Lv, Z. Lian, W. He, J. L. Sun, Q. Li and Q. Yan, *J. Mater. Chem. C*, 2018, **6**, 4464–4470.

70 A. L. Abdelhady, M. I. Saidaminov, B. Murali, V. Adinolfi, O. Voznyy, K. Katsiev, E. Alarousu, R. Comin, I. Dursun, L. Sinatra, E. H. Sargent, O. F. Mohammed and O. M. Bakr, *J. Phys. Chem. Lett.*, 2016, **7**, 295–301.

71 S. P. Sarmah, V. M. Burlakov, E. Yengel, B. Murali, E. Alarousu, A. M. El-Zohry, C. Yang, M. S. Alias, A. A. Zhumekenov, M. I. Saidaminov, N. Cho, N. Wehbe, S. Mitra, I. Ajia, S. Dey, A. E. Mansour, M. Abdelsamie, A. Amassian, I. S. Roqan, B. S. Ooi, A. Goriely, O. M. Bakr and O. F. Mohammed, *Nano Lett.*, 2017, **17**, 2021–2027.

72 I. Maeng, S. Lee, H. Tanaka, J.-H. Yun, S. Wang, M. Nakamura, Y.-K. Kwon and M.-C. Jung, *NPG Asia Mater.*, 2020, **12**, 53.

73 C. Rocks, V. Svrcek, P. Maguire and D. Mariotti, *J. Mater. Chem. C*, 2017, **5**, 902–916.

74 N. Rybin, D. Ghosh, J. Tisdale, S. Shrestha, M. Yoho, D. Vo, J. Even, C. Katan, W. Nie, A. J. Neukirch and S. Tretiak, *Chem. Mater.*, 2020, **32**, 1854–1863.

75 H. Shen, *J. Mater. Sci.*, 2019, **54**, 11596–11603.

76 J. Ding, Y. Zhao, S. Du, Y. Sun and H. Cui, *J. Mater. Sci.*, 2017, **52**, 7907–7916.

9950 | *J. Mater. Chem. C*, 2023, **11**, 9937–9951

This journal is © The Royal Society of Chemistry 2023

77 W. Wang, X. Wang, B. Zhang, Y. Guo and Q. Xu, *Phys. B*, 2020, **593**, 412310.

78 Y. Liu, Y. Zhang, K. Zhao, Z. Yang, J. Feng and X. Zhang, *Adv. Mater.*, 2018, **30**, 1707314.

79 T. Baikie, N. S. Barrow, Y. Fang, P. J. Keenan, P. R. Slater, R. O. Piltz, M. Gutmann, S. G. Mhaisalkar and T. J. White, *J. Mater. Chem. A*, 2015, **3**, 9298–9307.

80 X. Wang, Y. Li, Y. Xu, Y. Pan, C. Zhu, D. Zhu, Y. Wu, G. Li, Q. Zhang, Q. Li, X. Zhang, J. Wu, J. Chen and W. Lei, *Chem. Mater.*, 2020, **32**, 4973–4983.

81 Y. Zou, T. Zou, C. Zhao, B. Wang, J. Xing, Z. Yu, J. Cheng, W. Xin, J. Yang, W. Yu, H. Dong and C. Guo, *Small*, 2020, **16**, 2000733.

82 M. I. Saidaminov, V. Adinolfi, R. Comin, A. L. Abdelhady, W. Peng, I. Dursun, M. Yuan, S. Hoogland, E. H. Sargent and O. M. Bakr, *Nat. Commun.*, 2015, **6**, 8724.

83 R. Wang, S. Hu, X. Yang, X. Yan, H. Li and C. Sheng, *J. Mater. Chem. C*, 2018, **6**, 2989–2995.

84 I. S. Zhidkov, A. F. Akbulatov, M. I. Ustinova, A. I. Kukharenko, L. A. Frolova, S. O. Cholakh, C. C. Chueh, P. A. Troshin and E. Z. Kurmaev, *Coatings*, 2022, **12**, 1–7.

85 Y. Yamada, T. Yamada, L. Q. Phuong, N. Maruyama, H. Nishimura, A. Wakamiya, Y. Murata and Y. Kanemitsu, *J. Am. Chem. Soc.*, 2015, **137**, 10456–10459.

86 B. Wu, H. T. Nguyen, Z. Ku, G. Han, D. Giovanni, N. Mathews, H. J. Fan and T. C. Sum, *Adv. Energy Mater.*, 2016, **6**, 1600551.

87 S. Adjokatse, S. Shao, J. Even and M. A. Loi, *Nat. Commun.*, 2018, **9**, 243.

88 R. Murshed and S. Bansal, *Materials*, 2022, **15**, 899.

89 Y. Wu, L. Wan, S. Fu, W. Zhang, X. Li and J. Fang, *J. Mater. Chem. A*, 2019, **7**, 14136–14144.

90 Y. Mei, M. Sun, H. Liu, X. Li and S. Wang, *Org. Electron.*, 2021, **96**, 106258.

91 T.-H. Han, J.-W. Lee, C. Choi, S. Tan, C. Lee, Y. Zhao, Z. Dai, N. De Marco, S.-J. Lee, S.-H. Bae, Y. Yuan, H. M. Lee, Y. Huang and Y. Yang, *Nat. Commun.*, 2019, **10**, 520.

92 D. Shi, V. Adinolfi, R. Comin, M. Yuan, E. Alarousu, A. Buin, Y. Chen, S. Hoogland, A. Rothenberger, K. Katsiev, Y. Losovyj, X. Zhang, P. A. Dowben, O. F. Mohammed, E. H. Sargent and O. M. Bakr, *Science*, 2015, **347**, 519–522.

93 N. Parikh, P. Sevak, S. Jowhar Khanam, D. Prochowicz, S. Akin, S. Satapathi, M. M. Tavakoli, M. Banavoth, A. Kalam and P. Yadav, *ACS Omega*, 2022, **7**, 36535–36542.

94 S. J. Khanam, N. Parikh, S. Satapathi, A. Kalam, M. Banavoth and P. Yadav, *ACS Appl. Energy Mater.*, 2022, **5**, 14732–14738.

95 A. Bera, S. Bera, S. Kalimuddin, S. Gayen, M. Kundu, B. Das and M. Mondal, *Eur. Phys. J.: Spec. Top.*, 2021, **230**, 4113–4139.

96 M. B. Heindl, N. Kirkwood, T. Lauster, J. A. Lang, M. Retsch, P. Mulvaney and G. Herink, *Light: Sci. Appl.*, 2022, **11**, 31–33.

97 E. Roussel, C. Szwaj, C. Evain, B. Steffen, C. Gerth, B. Jalali and S. Bielawski, *Light: Sci. Appl.*, 2022, **11**, 14.

98 Y. Peng, C. Shi, Y. Zhu, M. Gu and S. Zhuang, *PhotoniX*, 2020, **1**, 12.

99 Z. Chen and M. Segev, *eLight*, 2021, **1**, 2.

100 X. Chen, H. Lindley-Hatcher, R. I. Stantchev, J. Wang, K. Li, A. Hernandez Serrano, Z. D. Taylor, E. Castro-Camus and E. Pickwell-MacPherson, *Chem. Phys. Rev.*, 2022, **3**, 011311.

101 L. Duvillaret, F. Garet and J. Coutaz, *IEEE J. Sel. Top. Quantum Electron.*, 1996, **2**, 739–746.

102 W. Withayachumnankul and M. Naftaly, *J. Infrared, Millimeter, Terahertz Waves*, 2014, **35**, 610–637.

103 E. J. Takahashi, Y. Nabekawa and K. Midorikawa, *Appl. Phys. Lett.*, 2004, **84**, 4–6.

104 E. Takahashi, Y. Nabekawa, T. Otsuka, M. Obara and K. Midorikawa, *Phys. Rev. A: At., Mol., Opt. Phys.*, 2002, **66**, 021802.

105 E. Constant, D. Garzella, P. Breger, E. Mével, C. Dorrer, C. Le Blanc, F. Salin and P. Agostini, *Phys. Rev. Lett.*, 1999, **82**, 1668–1671.

106 H. Hirori, P. Xia, Y. Shinohara, T. Otobe, Y. Sanari, H. Tahara, N. Ishii, J. Itatani, K. L. Ishikawa, T. Aharen, M. Ozaki, A. Wakamiya and Y. Kanemitsu, *APL Mater.*, 2019, **7**, 041107.

107 K. Nakagawa, H. Hirori, Y. Sanari, F. Sekiguchi, R. Sato and M. Saruyama, *Phys. Rev. Mater.*, 2021, **5**, 016001.

108 V. Strelkov, *Phys. Rev. Lett.*, 2010, **104**, 26–29.

109 N. Rosenthal and G. Marcus, *Phys. Rev. Lett.*, 2015, **133901**, 1–4.

110 P. B. Corkum, *Phys. Rev. Lett.*, 1993, **71**, 1994–1997.

111 M. Lewenstein, P. Balcou, M. Y. Ivanov, A. L'Huillier and P. B. Corkum, *Phys. Rev. A: At., Mol., Opt. Phys.*, 1994, **49**, 2117–2132.